processes

MDPI

Article

Mechanochemically and Sol–Gel Synthesized ZnO Catalysts for Advanced Tribocatalytic Degradation of Cephalexin

Trajce Trajkov [1], Stanislava Todorova [2] and Nina Kaneva [1,*]

[1] Laboratory of Nanoparticle Science and Technology, Department of General and Inorganic Chemistry, Faculty of Chemistry and Pharmacy, University of Sofia, 1 James Bourchier Blvd., 1164 Sofia, Bulgaria; trajce_trajkov11@hotmail.com

[2] Department of Applied Inorganic Chemistry, Faculty of Chemistry and Pharmacy, University of Sofia, 1 James Bourchier Blvd., 1164 Sofia, Bulgaria; nhtst@chem.uni-sofia.bg

* Correspondence: nina_k@abv.bg

Abstract

Cephalexin is a widely used antibiotic frequently detected in hospital wastewater and aquatic environments near pharmaceutical facilities, where its persistence contributes to the spread of antibiotic resistance. Mechanically driven advanced oxidation processes, including piezocatalysis and tribocatalysis, represent sustainable alternatives for pollutant removal because they operate without external light or heat sources. In this study, ZnO catalysts with controlled morphologies were synthesized via sol–gel and mechanochemical methods using different solvents and activation times (1 and 5 h). The influence of structural characteristics, surface area, and friction conditions on catalytic performance was systematically evaluated. The results demonstrated that tribocatalytic efficiency strongly depends on stirring rate and reactor material, with PTFE systems exhibiting superior performance. Mechanochemically activated ZnO (1 h) showed the highest degradation efficiency due to optimized defect density and surface accessibility. All catalysts exhibited high stability, while radical scavenging experiments identified superoxide radicals as the primary reactive species in the degradation process.

Keywords: ZnO; mechanochemical activation; tribocatalysis; piezocatalysis; cephalexin degradation

1. Introduction

Antibiotics are emerging organic contaminants that persist in the environment and threaten ecosystems and human health at elevated concentrations. Their main sources include pharmaceutical and personal care products and industrial effluents [1,2]. Continuous release contributes to antibiotic resistance, enabling bacteria to survive otherwise inhibitory concentrations. Even at low levels (μg/L), cephalexin shows measurable ecological effects [3]. Owing to their stability and insufficient removal by conventional treatment methods, antibiotics are often classified as persistent organic pollutants (POPs) [4].

Advanced oxidation processes (AOPs) provide efficient degradation pathways through the in situ generation of reactive oxygen species (ROS) with moderate energy demand. Among them, piezocatalysis [5–11] and tribocatalysis [12–16] have attracted increasing attention because they utilize mechanical energy to initiate catalytic reactions [17,18].

Piezocatalysis relies on the piezoelectric properties of non-centrosymmetric materials, which generate electric polarization under mechanical stress [9]. The induced charge

Check for updates

Academic Editor: Hikmat S. Hilal

Received: 28 April 2026
Revised: 18 May 2026
Accepted: 26 May 2026
Published: 28 May 2026

Copyright: © 2026 by the authors. Licensee MDPI, Basel, Switzerland. This article is an open access article distributed under the terms and conditions of the Creative Commons Attribution (CC BY) license.

separation promotes redox reactions: electrons reduce dissolved O_2 to superoxide radicals ($\bullet O_2^-$), while holes oxidize water or hydroxide ions to hydroxyl radicals (•OH) [9]. Recent works report improved charge separation efficiency via defect engineering and heterostructure design, significantly boosting catalytic activity [19,20]. Tribocatalysis operates through friction-induced charge transfer between contacting surfaces, similarly leading to the formation of $\bullet O_2^-$ and •OH radicals [21–24].

ZnO is widely investigated for mechanically induced catalysis due to its combined piezoelectric and triboelectric properties, wide band gap (~3.37 eV), low cost, abundance, and environmental compatibility [25,26]. Its catalytic performance strongly depends on morphology, surface area, and defect structure, and can be further improved through doping or composite formation [27]. Thermal annealing at 500 °C enhances crystallinity and charge mobility compared to non-annealed ZnO, resulting in improved degradation efficiency [28].

In addition to thermal treatment, mechanochemical activation represents an effective strategy to tailor ZnO properties. Mechanical milling or high-energy grinding can induce lattice distortion, generate oxygen vacancies, and increase surface defect density, thereby modifying electronic structure and enhancing catalytic activity [29,30]. Such mechanochemical processes improve surface reactivity and facilitate charge transfer during tribo- and piezocatalytic reactions. The introduction of structural defects through mechanoactivation can therefore promote more efficient ROS generation under mechanical stimulation [31,32].

Operational parameters such as reactor material, stirring speed, catalyst morphology, and synthesis conditions further influence degradation performance. The dominant ROSs are typically identified using radical scavengers such as isopropyl alcohol and ascorbic acid [33,34].

This work reviews the degradation of cephalexin using ZnO as both a tribocatalyst and piezocatalyst, with emphasis on mechanochemical activation, ROS generation pathways, and structure–performance relationships. The novelty of this study lies in the integrated analysis of thermal and mechanochemical modifications of ZnO and their combined influence on mechanically driven catalytic degradation. By systematically correlating structural defects, charge transfer behavior, and ROS formation, this work provides a comprehensive perspective on optimizing ZnO-based systems for enhanced antibiotic degradation.

2. Materials and Methods

Zinc acetate dihydrate ($Zn(CH_3COO)_2x2H_2O$, >99.5%), ethanol (C_2H_5OH, >99.0%), methanol (CH_3OH, >99.5%), and sodium hydroxide (NaOH, >99.0%) were sourced from Fluka (Buchs, Switzerland). Distilled water was employed in all experiments, and all other chemicals and reagents were of analytical grade.

Cephalexin ($C_{16}H_{17}N_3O_4S$, λ_{max} = 262 nm, Teva, Troyan, Bulgaria) was used as a model contaminant in all tribocatalytic experiments. Cephalexin is a widely prescribed β-lactam antibiotic frequently detected in hospital effluents and surface waters due to its extensive consumption and incomplete removal in conventional wastewater treatment systems [35]. Its persistence in aquatic environments raises environmental concerns, as continuous exposure may contribute to the development of antibiotic-resistant bacteria and ecological imbalance. Beyond environmental implications, cephalexin may also induce adverse physiological effects when present at elevated concentrations. Reported side effects include increased liver enzyme levels, thrombocytopenia (reduced platelet count), and eosinophilia, reflecting its potential hematological and hepatic impact [36]. These findings further justify the need for efficient degradation strategies.

The catalytic experiments were designed to evaluate the degradation behavior of cephalexin under mechanically induced conditions. Distilled water was used as the reaction

medium to simulate simplified aquatic systems, allowing controlled assessment of catalyst performance in the presence of dissolved species.

ZnO nanoparticles were synthesized via a sol–gel method using zinc acetate dihydrate ($Zn(CH_3COO)_2x2H_2O$) as a precursor and sodium hydroxide (NaOH) as a precipitating agent. Two different alcohol solvents—methanol and ethanol—were employed in order to evaluate the influence of solvent type on nucleation, growth kinetics, and final morphology. For the methanol-based system, 1.09 g of $Zn(CH_3COO)_2x2H_2O$ was dissolved in 50 mL of methanol under continuous magnetic stirring (500 rpm) at room temperature until a clear and homogeneous solution was obtained. In parallel, a second precursor solution was prepared using ethanol as solvent. Due to the lower solubility of $Zn(CH_3COO)_2{\cdot}2H_2O$ in ethanol, 0.05 g of the salt was dissolved in 50 mL of ethanol under identical stirring conditions.

A NaOH solution was prepared separately for each solvent system. For the ethanolic route, 0.22 g of NaOH was dissolved in 25 mL of ethanol. Because of the limited solubility of NaOH in absolute ethanol, 8 mL of deionized water was added to facilitate complete dissolution and ensure uniform alkalinity. For the methanolic route, the same amount of NaOH (0.22 g) was dissolved directly in methanol without the addition of water, as sufficient solubility was achieved under stirring.

After complete dissolution of the reagents, the NaOH solution was added dropwise to the corresponding zinc acetate solution under continuous stirring. The gradual addition promoted controlled hydrolysis of Zn^{2+} ions and subsequent condensation reactions, leading to the formation of $Zn(OH)_2$ intermediates, which transformed into ZnO nuclei. The reaction mixture became turbid, indicating particle formation. Stirring was maintained to ensure homogeneous nucleation and growth throughout the solution. The obtained suspensions were denoted as ZnO/EtOH and ZnO/MeOH, according to the solvent used during synthesis. The influence of solvent polarity and water content on hydrolysis rate, particle growth, and defect formation was considered critical for tailoring the structural and catalytic properties of the resulting ZnO powders.

Mechanochemical activation was performed using a Fritsch Pulverisette 5 mill. The samples were ground for 5 h at a ball to powder mass ratio of 20:1 and a rotation speed of 500 rpm, under dry conditions. The grinding was divided into cycles of one hour followed by a pause of 15 min.

The synthesized samples were comprehensively characterized to assess their morphology, microstructure, crystallinity, and optical properties. Scanning electron microscopy (Zeiss Evo 15, Bruker, Resolution 126 eV, Berlin, Germany) coupled with energy-dispersive X-ray spectroscopy (EDS, Tokyo, Japan) was used to examine surface morphology and elemental composition. Phase identification and crystallinity were determined by X-ray diffraction with Cu-Kα (1.5418 Å) radiation (Empyrean, Malvern Panalytical X-ray diffractometer, Malvern, UK), at a step of $2\theta = 0.05^\circ$ and counting time 4 s/step. The mean crystallite sizes are calculated using Scherrer's equation for 101 peak of ZnO [37]. Room-temperature photoluminescence (PL) spectra were recorded on a Varian Cary Eclipse Fluorescence UV–Vis spectrophotometer (excitation wavelength 325 nm).

Tribocatalysis was applied to degrade a 50 mL solution of Cephalexin. The drug was prepared in a 100 mL beaker using distilled water and a magnetic stirrer. The tribocatalytic experiments were conducted at a constant room temperature of 23 ± 2 °C under dark conditions. The initial antibiotic concentration was 15 ppm. Fifty milligrams of sol–gel or mechanically synthesized ZnO catalyst was added to the solution, and the resulting suspension was stirred with a polytetrafluoroethylene (PTFE)-coated magnetic rod. The mixture was allowed to equilibrate for 30 min without stirring to ensure adsorption equilibrium between the tribocatalyst and the Cephalexin molecules. Following this, the tribocatalytic

reaction was initiated at a constant stirring speed of 100 rpm. The piezocatalytic experiments were carried out under identical experimental conditions, with the only difference being the type of magnetic stirring rod used, namely a glass-coated magnetic rod instead of a PTFE-coated one.

Aliquots of 2 mL were periodically withdrawn from the reaction mixture, and the catalyst was separated by centrifugation at 6000 rpm. Except for variations in magnetic stirring conditions (300 and 500 rpm), and beaker material (glass or PTFE), all other experimental conditions were maintained consistently across the degradation tests. Enhanced tribocatalytic efficiency was observed in PTFE-based setups, attributed to increased electron generation upon contact with the PTFE stirrer and beaker. All catalytic degradation experiments were performed in triplicate to ensure the reproducibility and reliability of the obtained results. The degradation curves and kinetic parameters presented in the manuscript correspond to the arithmetic mean values of the three independent experiments.

The UV–Vis spectra of Cephalexin in the 200–600 nm range were recorded using an Evolution 300 spectrophotometer (Thermo Scientific, Madison, WI, USA). The contribution of reactive species to the degradation process was assessed via scavenger tests. Ethylenediaminetetraacetic acid disodium salt (EDTA-2Na), isopropyl alcohol (IPA), and ascorbic acid (AA) were employed as scavengers for holes, superoxide, and hydroxyl radicals, respectively. To identify the specific reactive species responsible for the tribocatalytic degradation of Cephalexin, 6 mg of each scavenger was tested separately in the 50 mL drug solution.

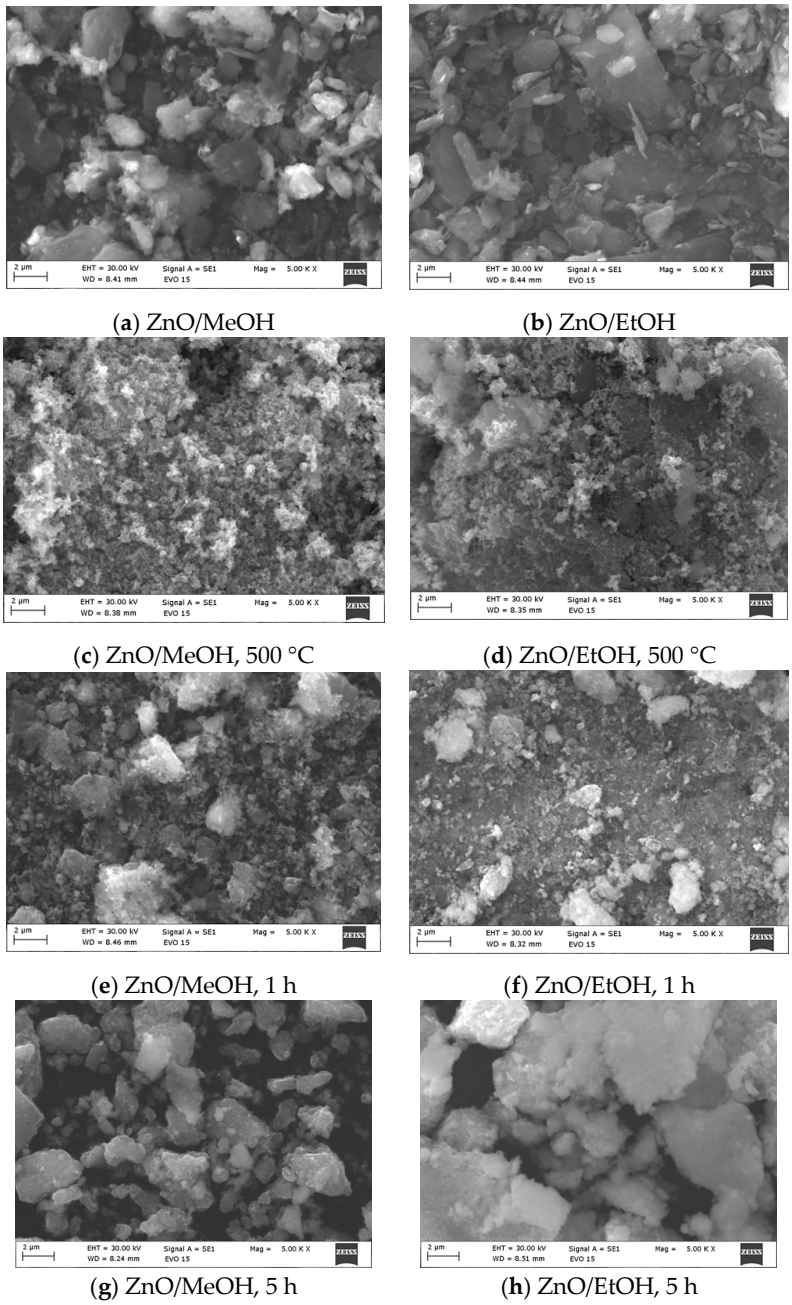
3. Results and Discussion

3.1. Structural and Morphological Characterization of ZnO Samples

Figure 1a–d illustrates the morphology of sol–gel synthesized ZnO powders prepared using two different solvents—methanol and ethanol—before and after annealing at 500 °C. In the non-annealed samples, (Figure 1a) ZnO/MeOH and (Figure 1b) ZnO/EtOH, pronounced agglomeration of irregularly shaped primary particles is observed. The methanol-derived sample (Figure 1a) is characterized by larger, densely packed aggregates with relatively smooth surfaces and limited porosity. In contrast, the ethanol-derived sample (Figure 1b) exhibits a more heterogeneous morphology, including elongated and plate-like crystallites. Following calcination at 500 °C (Figure 1c,d), significant morphological evolution occurs. In both cases, a more finely dispersed and highly porous structure develops as a result of the thermal decomposition of organic residues and ZnO crystallization. The ZnO/MeOH sample (Figure 1c) shows a relatively uniform distribution of nanoparticles with increased surface roughness and a well-developed microporous texture. In comparison, the ZnO/EtOH sample (Figure 1d) remains more heterogeneous, with the presence of larger aggregates, suggesting a partial reduction in specific surface area. These morphological differences directly affect the catalytic performance of the materials in cephalexin degradation. The higher specific surface area, increased surface roughness, and greater density of defect sites in the annealed ZnO/MeOH sample enhance antibiotic adsorption and promote the generation of reactive oxygen species (ROS), resulting in improved catalytic activity. Conversely, the more agglomerated structure of ZnO/EtOH limits the accessibility of active sites, potentially reducing the overall process efficiency.

The SEM images illustrate the morphology of ZnO particles obtained after mechanochemical activation in different liquid media and milling durations: ZnO/MeOH (Figure 1e) and ZnO/EtOH (Figure 1f) after 1 h, and ZnO/MeOH (Figure 1g) and ZnO/EtOH (Figure 1h) after 5 h of treatment. At shorter activation time (1 h; Figure 1e,f), the samples consist of relatively well-dispersed particles with irregular morphology and a broad size distribution. The degree of agglomeration is limited, and individual grains can still be distinguished, particularly in the ZnO/EtOH sample (Figure 1f), where a more homogeneous dispersion is observed. Upon

increasing the activation time to 5 h (Figure 1g,h), significant morphological changes occur, characterized by pronounced agglomeration of particles, leading to the formation of larger, more compact aggregates. This effect is especially evident for ZnO/EtOH (Figure 1h), where dense clusters with reduced surface heterogeneity are formed. The prolonged mechanochemical treatment in the ball mill induces structural rearrangement and partial sintering-like behavior, resulting in the transformation from loosely packed fine particles into strongly fused agglomerates. Such agglomeration is attributed to the increased mechanical energy input, which enhances surface diffusion and interparticle bonding, ultimately reducing the specific surface area and the number of accessible active sites. These morphological changes have a direct impact on the tribocatalytic performance of the materials, leading to decreased efficiency in the degradation of cephalexin due to the limited accessibility of reactive surface sites.



(**a**) ZnO/MeOH (**b**) ZnO/EtOH

(**c**) ZnO/MeOH, 500 °C (**d**) ZnO/EtOH, 500 °C

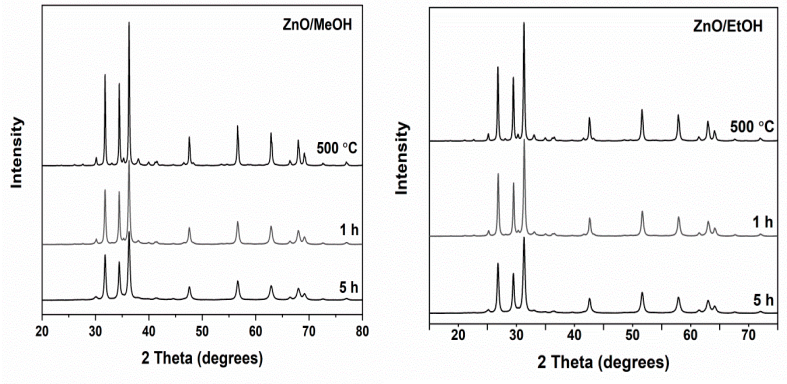
(**e**) ZnO/MeOH, 1 h (**f**) ZnO/EtOH, 1 h

(**g**) ZnO/MeOH, 5 h (**h**) ZnO/EtOH, 5 h

Figure 1. SEM micrographs of ZnO sol–gel (**a**,**b**—nonannealed; **c**,**d**—annealed) and powders after mechanochemically activated in methanol (MeOH) and ethanol (EtOH) for 1 h (**e**,**f**) and 5 h (**g**,**h**).

The SEM observations are consistent with the BET surface area analysis, which revealed slightly higher specific surface areas for the ZnO powders subjected to short-term mechanochemical activation (12.2 m^2/g for MeOH and 11.6 m^2/g for EtOH, 1 h), likely due to particle refinement and increased surface accessibility. In contrast, prolonged mechanochemical treatment (5 h) resulted in lower BET surface areas (8.8 m^2/g for MeOH and 8.0 m^2/g for EtOH), which can be attributed to the formation of densely agglomerated particle clusters observed in the SEM micrographs. The annealed samples exhibited intermediate BET values of 10.8 m^2/g and 9.5 m^2/g for the MeOH- and EtOH-treated powders, respectively.

The XRD patterns presented in Figure 2 confirm that all synthesized and mechanochemically treated samples crystallize in the hexagonal wurtzite structure of ZnO (space group $P6_3mc$), in accordance with the standard diffraction data reported in JCPDS card No. 36-1451. The diffraction peaks located at 2θ values of approximately 31.7°, 34.4°, and 36.2° are assigned to the (100), (002), and (101) crystallographic planes, respectively, which are characteristic reflections of crystalline ZnO. No additional diffraction peaks related to secondary phases, impurities, or residual precursor compounds were detected within the instrumental sensitivity, indicating the successful formation of phase-pure ZnO in all investigated samples [38]. The annealed samples synthesized in methanol and ethanol media (ZnO/MeOH, 500 °C and ZnO/EtOH, 500 °C; Figure 2a,b) exhibit sharp, narrow, and highly intense diffraction peaks, suggesting a high degree of crystallinity and the formation of well-ordered crystal domains [39]. A slight difference in peak profile is observed between the two solvent systems. In particular, the methanol-derived ZnO displays relatively narrower and more intense reflections compared with the ethanol-derived counterpart, indicating larger crystallite dimensions and lower structural disorder. This behavior can be associated with the physicochemical properties of methanol, such as its lower viscosity and higher polarity, which facilitate faster hydrolysis and nucleation kinetics during synthesis, followed by more homogeneous crystal growth during thermal treatment [40]. In contrast, ethanol provides a comparatively slower nucleation and growth environment due to its lower polarity and higher viscosity, which may contribute to the formation of smaller crystallites and a slightly higher concentration of structural imperfections and lattice disorder [41].



(**a**) (**b**)

Figure 2. X-ray diffraction (XRD) patterns of ZnO samples synthesized via sol–gel method using methanol (**a**) and ethanol (**b**) as solvents, followed by thermal treatment at 500 °C and subsequent mechanochemically activated (1 and 5 h).

After mechanochemical activation for 1 h and 5 h, noticeable changes in the diffraction profiles are observed for both solvent-derived ZnO systems. Specifically, progressive broadening of the diffraction peaks accompanied by a decrease in peak intensity occurs with increasing milling duration. Such changes are typically associated with a reduction

in crystallite size, partial loss of long-range crystallographic order, and the accumulation of microstrain within the ZnO lattice [42]. In addition, high-energy mechanical treatment can introduce various structural defects, including oxygen vacancies, zinc interstitials, and surface disorder, which contribute to lattice distortion and enhanced defect density [43]. The effect becomes increasingly pronounced after 5 h of mechanochemical activation, demonstrating the substantial influence of mechanical milling on the structural evolution of ZnO particles. Nevertheless, despite the observed peak broadening and crystallinity reduction, all diffraction peaks remain indexed to the wurtzite ZnO phase, confirming that no phase transformation or amorphization occurs during the applied mechanochemical treatment [44].

The average crystallite size (d) of the investigated samples was estimated using the Scherrer equation based on the most intense diffraction reflections. The calculated values are summarized in Table 1 and reveal a systematic decrease in crystallite size after mechanochemical activation. The crystallite size decreases from 86 nm for ZnO/MeOH, 500 °C, and 76 nm for ZnO/EtOH, 500 °C, to 60 and 63 nm after 1 h of milling, respectively, and further decreases to 48 and 49 nm after 5 h of mechanochemical treatment. This gradual reduction in crystallite size correlates well with the observed peak broadening in the XRD patterns and confirms the fragmentation of crystalline domains induced by mechanical milling. The reduction in crystallite size and the simultaneous increase in structural defect concentration are expected to significantly influence the catalytic behavior of ZnO. Smaller crystallites provide a larger specific surface area and a greater number of exposed active surface sites, which can facilitate adsorption and interfacial redox reactions. Moreover, the presence of lattice defects, particularly oxygen vacancies, can act as charge trapping centers that suppress rapid electron–hole recombination and enhance charge separation efficiency [45]. These structural modifications are highly beneficial for catalytic processes involving reactive oxygen species (ROS), as they promote the generation of hydroxyl (•OH) and superoxide ($\bullet O_2^-$) radicals responsible for pollutant degradation. The obtained results further demonstrate that the solvent used during synthesis plays an important role in determining the initial structural characteristics of ZnO, particularly crystallinity and crystallite size. Methanol-derived samples exhibit larger and more ordered crystallites after calcination, whereas ethanol-derived ZnO shows comparatively smaller crystal domains. However, following prolonged mechanochemical activation, the structural differences between the two solvent systems become considerably less pronounced, suggesting that mechanical treatment becomes the dominant factor controlling crystallite refinement, defect formation, and structural modification. Therefore, the combined application of solvent-controlled synthesis and mechanochemical activation represents an effective approach for tailoring the structural and catalytic properties of ZnO materials toward enhanced catalytic and ROS-mediated degradation performance.

Table 1. Band gap energies and crystallite sizes of sol–gel and mechanochemically activated ZnO powders.

Samples	Band Gap, eV	Crystallite Size, nm
ZnO/MeOH, sol–gel	3.25	86
ZnO/EtOH, sol–gel	3.27	76
ZnO/MeOH, 1h	3.25	60
ZnO/EtOH, 1 h	3.28	63
ZnO/MeOH, 5 h	3.26	48
ZnO/EtOH, 5 h	3.27	49

3.2. Optical Properties and Electronic Structure

Ultraviolet–visible (UV–Vis) absorption spectroscopy was employed to investigate the optical properties of the synthesized semiconductor materials, as this technique is widely applied for assessing the optical behavior of solid-state systems. The band gap energies of the powder samples were determined via Kubelka–Munk function extrapolation, as shown in Figure 3. The estimated band gap values for the sol–gel-derived samples are 3.25 eV for ZnO/MeOH and 3.27 eV for ZnO/EtOH, while for the mechanoactivated samples, the values are 3.25 eV (ZnO/MeOH) and 3.28 eV (ZnO/EtOH). A consistent trend is observed in both synthesis approaches, where the use of methanol as a solvent results in slightly reduced band gap energies.

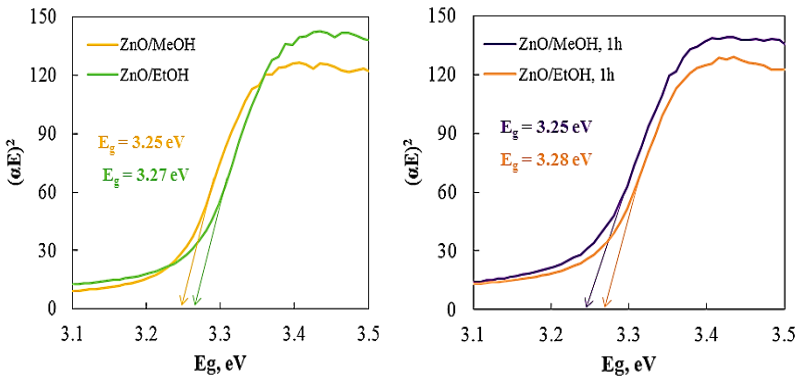


Figure 3. Band gap energies of sol–gel (**a**) and mechanoactivated (**b**) ZnO powders prepared with methanol and ethanol.

This narrowing of the band gap can be attributed to an increased density of structural defects, such as oxygen vacancies, as well as enhanced microstrain and lattice distortions induced during synthesis. These factors introduce localized energy states within the band structure, facilitating electronic transitions at lower energies. As a result, the reduced band gap contributes to more efficient generation of charge carriers, which is directly linked to enhanced tribocatalytic activity of the materials.

The photoluminescence (PL) emission spectra were employed to evaluate the efficiency of charge carrier trapping, charge transfer processes, and the presence of surface defects. In addition, the PL spectra provided insight into the behavior of photoinduced electron–hole pairs in the synthesized metal oxide semiconductor material. The photoluminescence measurements were conducted at room temperature using an excitation wavelength of 325 nm (UV-A region), as illustrated in the figure. During the tribocatalytic process, the recombination of mechanically generated electron–hole pairs, accompanied by photon emission, was observed and can be attributed to the radiative relaxation of excited zinc-related species induced by frictional energy input. The PL spectra of zinc oxide samples synthesized via the sol–gel method and subjected to subsequent mechanochemical activation reveal significant differences in their optical emission behavior, which can be attributed to variations in defect structure and crystallinity. The PL spectra of the as-prepared sol–gel samples (Figure 4a) exhibit two principal emission regions. A relatively weak, broad ultraviolet (UV) emission band is observed at approximately 370–380 nm, corresponding to excitonic recombination. In contrast, a pronounced, broad visible emission band centered at 520–530 nm is detected commonly attributed to deep-level defects, predominantly oxygen vacancies and related intrinsic defects. The dominance of this green emission suggests a relatively high concentration of structural defects and incomplete crystallization in the sol–gel-derived ZnO. Minor differences between samples prepared using methanol and

ethanol as solvents are observed, mainly in emission intensity, indicating that the choice of solvent influences defect density and particle morphology, likely due to differences in hydrolysis and condensation kinetics during synthesis.

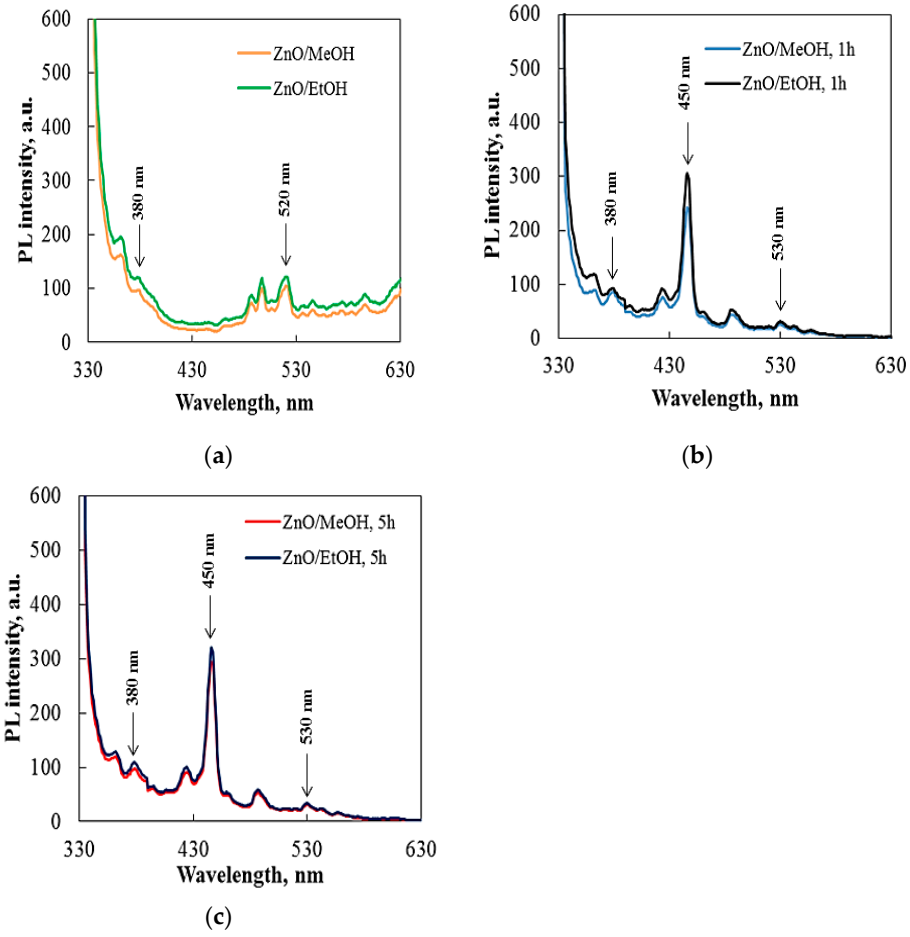


Figure 4. Photoluminescence spectra of (**a**) sol–gel and mechanochemically activated ZnO powders treated in methanol (MeOH) and ethanol (EtOH) for (**b**) 1 h and (**c**) 5 h.

The photoluminescence spectra of ZnO powders subjected to mechanochemical activation in the presence of methanol (MeOH) and ethanol (EtOH) for 1 h and 5 h are shown in Figure 4b,c. The PL analysis provides insights into the defect structures and recombination processes, which are closely related to the tribocatalytic performance of the materials. All samples show an emission in the UV region (about 330–350 nm), corresponding to excitonic recombination in ZnO. This emission confirms that the crystalline phase is preserved after mechanochemical treatment. However, a noticeable decrease in intensity is observed with longer milling times, indicating a partial loss of crystallinity or an increase in non-radiative recombination pathways caused by prolonged mechanical activation. In the visible region, a broad emission band centered around 430–450 nm is detected in all samples. This band is typically attributed to intrinsic defects, such as oxygen vacancies and zinc interstitials, as well as surface states. The presence of these defect-related emissions indicates that mechanochemical treatment effectively creates defect sites, which can act as active centers in catalytic processes. A closer comparison shows that the PL intensity in the visible region is higher for samples treated with ethanol after 1 h of milling, suggesting a higher concentration of radiative defect centers. However, this does not necessarily correlate with improved catalytic activity. In fact, the MeOH-treated samples demonstrate better tribocatalytic performance in degrading cephalexin, indicating that not just defect

quantity but also the type and accessibility of defect sites are crucial. Moreover, extending the milling time to 5 h results in similar PL spectra for both solvents, suggesting that the influence of the solvent diminishes compared to the dominant effect of mechanical treatment. Despite an apparent increase in defect-related emission, the tribocatalytic activity of these samples declines. This behavior can be explained by considering both electronic and morphological factors. Although longer milling promotes defect formation, it also leads to particle agglomeration, as confirmed by morphological analysis. The powders activated for 5 h show a higher degree of agglomeration, reducing the effective surface area and limiting active site accessibility. Excessive defect concentration may also promote charge carrier recombination, thereby decreasing reactive oxygen species (ROS) generation efficiency. In contrast, the samples milled for 1 h, especially those treated with methanol; strike a better balance between crystallinity and defect density while maintaining a less agglomerated morphology. This results in improved charge separation and more efficient ROS generation under tribocatalytic conditions, ultimately leading to higher degradation rates. The combined PL and morphological analyses show that optimal tribocatalytic performance occurs at shorter milling times and with methanol-assisted activation. The findings highlight that defect concentration and type, charge recombination dynamics, and particle morphology collectively influence the effectiveness of ZnO-based tribocatalysts.

The results demonstrate that mechanochemical activation plays a crucial role in tailoring the defect landscape of ZnO. While sol–gel synthesis favors the formation of deep-level defects responsible for green luminescence, mechanical treatment promotes the generation of shallow defect states and modifies the relative contribution of radiative recombination pathways. These findings highlight the strong correlation between processing conditions, defect structure, and optical properties, which is essential for the design of ZnO-based materials for tribocatalytic applications.

3.3. Tribocatalytic Degradation of Cephalexin Using Sol–Gel ZnO Powders: Effect of Solvent and Stirring Rate

The tribocatalytic degradation of cephalexin was investigated using sol–gel synthesized, non-annealed ZnO as a catalyst. The material was prepared using two different solvents, methanol and ethanol, in order to evaluate the influence of solvent-assisted synthesis on catalytic performance. Particular attention was given to the role of hydrodynamic conditions and solvent properties in governing the degradation efficiency. Tribocatalysis—an advanced oxidation process driven by friction-induced charge separation—has been demonstrated as a sustainable method for the degradation of organic pollutants, including antibiotics, in aqueous environments [46].

Figure 5a presents the tribocatalytic degradation of cephalexin as a function of solvent (methanol and ethanol) and stirring rate. At low rotation speed (100 rpm), the process is kinetically limited, as reflected by the relatively low apparent rate constants of 0.0263 h^{-1} for ZnO/MeOH and 0.0138 h^{-1} for ZnO/EtOH. The reduced efficiency is attributed to limited interfacial contact and insufficient generation of reactive oxygen species (ROS), consistent with observations in related tribocatalytic systems [47]. A consistent solvent effect is observed across all studied conditions, with methanol outperforming ethanol. This behavior is associated with the lower molecular weight and higher polarity of methanol, which facilitate improved dispersion of ZnO particles, enhanced charge transfer, and the formation of more reactive radical species [48]. In contrast, ethanol forms less reactive species and exhibits less favorable mass transport properties.

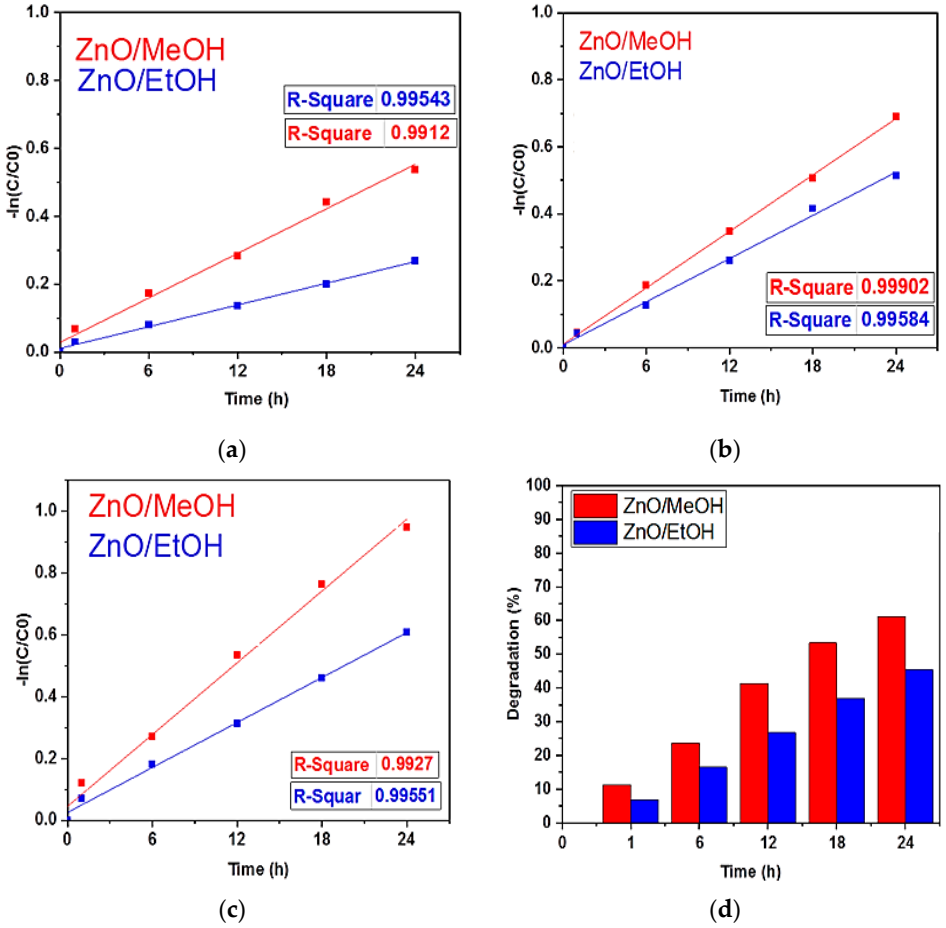


Figure 5. Tribocatalysis of Cephalexin at different stirring speed (**a**) 100, (**b**) 300 and (**c**) 500 rpm using non-annealed ZnO powders, (**d**) Degree of degradation of Cephalexin.

Increasing the stirring rate to 300 rpm (Figure 5b) results in a noticeable enhancement of the degradation kinetics, with rate constants rising to 0.0325 h^{-1} (ZnO/MeOH) and 0.0229 h^{-1} (ZnO/EtOH). A further increase to 500 rpm (Figure 5c) leads to a substantial improvement, reaching 0.0495 h^{-1} and 0.0314 h^{-1} for methanol and ethanol, respectively. This trend indicates that tribocatalytic efficiency is strongly dependent on hydrodynamic conditions, as has been reported in studies varying stirring speed in ZnO tribocatalysis [47].

The enhancement at higher stirring rates can be attributed to intensified frictional interactions between the tribocatalyst particles, promoting charge separation and electron transfer. In parallel, improved mixing enhances mass transport, reduces diffusion limitations, and increases the frequency of effective collisions between reactive species and cephalexin molecules [48]. These effects collectively result in increased ROS generation and accelerated degradation kinetics.

The observed kinetic trends are consistent with the experimentally determined degradation efficiencies (Figure 5d). At 100 rpm, removal percentages of 41.61% (ZnO/MeOH) and 24.76% (ZnO/EtOH) were obtained, corresponding to the lower rate constants. At 300 rpm, the degradation increased to 49.82% and 40.12% for methanol and ethanol, respectively, in agreement with the higher kinetic values. The highest efficiencies were achieved at 500 rpm, reaching 61.19% (ZnO/MeOH) and 45.48% (ZnO/EtOH), which further confirms the direct correlation between the apparent rate constants and the degradation performance. This agreement supports the validity of the kinetic analysis and demonstrates that the reaction follows consistent pseudo-first-order behavior under the studied conditions [49]. The results demonstrate that both solvent properties and stirring rate play a decisive role

in tribocatalytic performance, with methanol and higher rotation speeds (300–500 rpm) providing optimal conditions for efficient cephalexin degradation.

3.4. Tribocatalytic Degradation of Cephalexin Using Sol–Gel ZnO Powders: Effect of Thermal Annealing and Reactor Material

The structure and morphology of ZnO tribocatalysts play a critical role in cephalexin degradation. Parameters such as particle size, crystallinity, surface roughness, and defect density govern charge carrier generation, separation, and transfer to reactive species [50,51]. Highly crystalline ZnO with reduced defect density—typically achieved via thermal annealing—suppresses electron–hole recombination, thereby enhancing charge availability for oxidative reactions and improving degradation efficiency.

Annealing further promotes grain growth (Figure 1) and partial between particles, enhancing mechanical stability, interparticle contact, and interactions with the PTFE stirring rod. These effects intensify triboelectric charge generation. Additionally, increased surface roughness enlarges the effective contact area, strengthening local electric fields and facilitating the formation of reactive oxygen species (ROS), such as hydroxyl (•OH) and superoxide ($\bullet O_2^-$) radicals, which drive the cleavage of the β-lactam ring in cephalexin. Catalyst morphology also influences adsorption behavior. Well-dispersed nanostructures with high surface area provide more active sites, enhancing pollutant adsorption and interaction with ROS, whereas highly defective structures may act as charge traps and reduce catalytic efficiency.

Kinetic analysis supports these observations, confirming the superior tribocatalytic activity of annealed samples compared to non-annealed ones, as evidenced by higher rate constants and degradation efficiencies (Table 1). In the degradation of Cephalexin, annealed samples has a k value 1.5 times greater than that of non-annealed. Thus, annealed catalysts exhibits greater tribocatalytic activity for degradation of antibiotic. The same trend is observed for the annealed powders, the samples prepared with methanol possess higher catalytic efficiency. At an agitation speed of 500 rpm (Table 2), the ZnO/MeOH system exhibits a higher apparent rate constant than ZnO/EtOH, indicating more efficient degradation. High R^2 values (>0.99) confirm excellent agreement with the kinetic model [52]. The lower agitation rates (100 rpm) affect weaker triboelectric interactions and lower ROS generation [53].

Table 2. Rate constants and degree of decomposition of Cephalexin using non-annealed and annealed ZnO samples.

Samples			100 rpm		300 rpm		500 rpm	
			k, h^{-1}	D%	k, h^{-1}	D%	k, h^{-1}	D%
ZnO/MeOH	**Glass beaker**	non-annealed	0.0263 h^{-1}	41.61%	0.0325 h^{-1}	49.82%	0.0495 h^{-1}	61.19%
		annealed	0.0362 h^{-1}	52.38%	0.0527 h^{-1}	67.02%	0.0746 h^{-1}	78.81%
	PTFE beaker	non-annealed	0.0363 h^{-1}	51.61%	0.0499 h^{-1}	61.85%	0.0651 h^{-1}	73.69%
		annealed	0.0516 h^{-1}	63.57%	0.0648 h^{-1}	71.55%	0.0924 h^{-1}	86.61%
ZnO/EtOH	**Glass beaker**	non-annealed	0.0138 h^{-1}	24.76%	0.0229 h^{-1}	40.12%	0.0314 h^{-1}	45.48%
		annealed	0.0282 h^{-1}	44.52%	0.0325 h^{-1}	51.37%	0.0437 h^{-1}	60%
	PTFE beaker	non-annealed	0.0222 h^{-1}	37.32%	0.0329 h^{-1}	47.86%	0.0436 h^{-1}	58.33%
		annealed	0.0373 h^{-1}	53.69%	0.047 h^{-1}	63.04%	0.0656 h^{-1}	73.51%

Following the observation that annealed ZnO samples exhibited higher activity in glass reactor tests, the effect of reactor material was investigated. Comparisons between glass and PTFE reactors revealed that the PTFE reactor enhanced tribocatalytic performance. At 500 rpm, cephalexin degradation in the PTFE reactor reached 86.61% for ZnO/MeOH and 73.51% for ZnO/EtOH; at 300 rpm, 71.55% and 63.04%; and at 100 rpm, 63.57% and

53.69%, respectively. The superior performance of the PTFE reactor can be attributed to its higher triboelectric potential relative to glass. During stirring, the stronger triboelectric interaction between ZnO particles and the PTFE surface promotes more effective charge transfer, increasing the generation of ROS such as hydroxyl (•OH) and superoxide ($\bullet O_2^-$) radicals. Additionally, the lower surface energy and chemical inertness of PTFE reduce particle aggregation and facilitate more uniform particle–surface contact, which further enhances localized electric fields and charge separation. These combined effects lead to higher ROS formation and more efficient oxidative degradation of cephalexin compared to glass reactors. These findings highlight that both catalyst morphology and reactor material significantly influence tribocatalytic efficiency, with annealed ZnO in PTFE reactors providing the optimal combination for maximizing cephalexin degradation.

Radical scavenging experiments provide a direct means of evaluating the contribution of reactive oxygen species (ROS) to tribocatalytic activity and comparing the performance of different reactor materials. In this study, the effects of adding ascorbic acid (AA), isopropyl alcohol (IPA), and EDTA-2Na to the two tribocatalyst systems (ZnO/MeOH and ZnO/EtOH) in glass and PTFE reactors were investigated (Figure 6). In the absence of scavengers, the degradation efficiency ranged from approximately 82–90% for ZnO/MeOH to 62–78% for ZnO/EtOH, depending on the reactor material. The addition of AA resulted in the most pronounced suppression of tribocatalytic activity, decreasing the degradation efficiency to about 66–75% for ZnO/MeOH and 48–60% for ZnO/EtOH. In comparison, the presence of IPA and EDTA-2Na caused a less significant reduction, with degradation efficiencies remaining within the ranges of 76–86% and 58–74%, respectively. The stronger inhibitory effect of AA compared to IPA and EDTA-2Na demonstrates that superoxide radicals ($\bullet O_2^-$) play a more prominent role in cephalexin degradation than hydroxyl radicals (•OH) or photogenerated holes (h^+). By selectively quenching the corresponding reactive species, the experiments enabled the relative contributions of $\bullet O_2^-$, •OH, and h^+ to be evaluated, confirming that $\bullet O_2^-$ radicals predominantly govern the breakdown of the antibiotic under the tested tribocatalytic conditions. These findings complement the observed higher degradation efficiencies in PTFE reactors compared to glass reactors. The enhanced tribocatalytic activity in PTFE reactors can be attributed not only to stronger frictional interactions and improved charge transfer but also to more effective generation and utilization of reactive oxygen species, particularly superoxide radicals. Together, these results highlight the combined influence of reactor material and ROS generation pathways on the overall tribocatalytic performance.

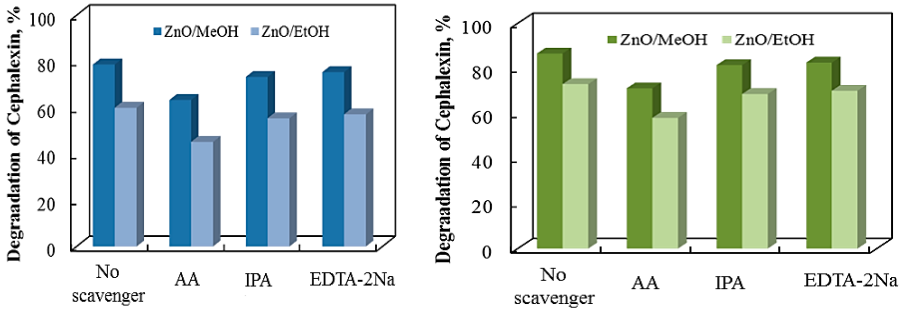


Figure 6. Radical scavengers (ascorbic acid and isopropyl alcohol) on cephalexin degradation by ZnO/MeOH and ZnO/EtOH in (**a**) glass and (**b**) PTFE reactors.

Figure 7 presents the results of a five-cycle recyclability study of ZnO/MeOH and ZnO/EtOH tribocatalysts conducted in glass and PTFE reactors. A slight decrease in the tribocatalytic degradation efficiency of cephalexin was observed after successive cy-

cles, with an overall reduction of approximately 5% after the third run in distilled water for all catalyst systems. This minor decline indicates a small loss of catalytic activity upon reuse, likely associated with surface fouling or partial deactivation of active sites during operation.

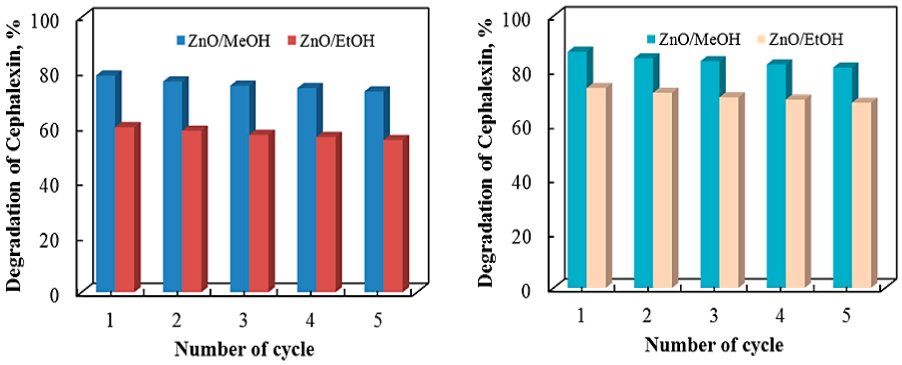


Figure 7. Stability and reusability of annealed ZnO/MeOH and ZnO/EtOH catalysts in repeated tribocatalytic degradation tests (three cycles) in (**a**) glass and (**b**) PTFE reactors.

Nevertheless, the sol–gel-derived samples demonstrated good stability throughout the cycling experiments, maintaining a high level of degradation efficiency. These results confirm the satisfactory reusability of the materials and highlight their potential for repeated application in cephalexin removal. The limited performance loss suggests that the catalysts retain their structural integrity and do not undergo significant changes or mechanical degradation during the tribocatalytic process. This stability is a key factor for practical applications, where long-term operation and cost-effectiveness are essential.

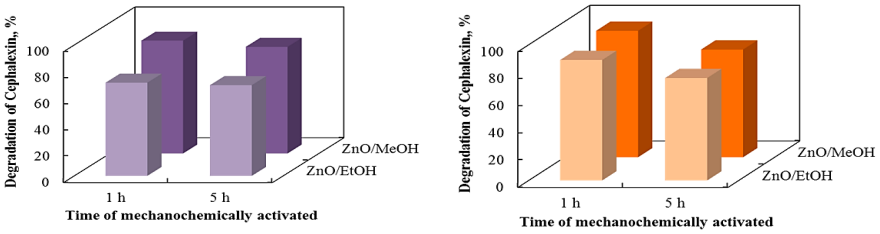
3.5. Tribocatalytic Degradation of Cephalexin Using Mechanochemically Activated ZnO Powders

Following the evaluation of the thermally treated sol–gel-derived ZnO samples, further improvement of the catalytic performance was pursued via mechanochemical activation. This approach was employed to enhance the surface morphology and increase the density of active sites, thereby improving the tribocatalytic efficiency. Mechanochemical treatment by high-energy ball milling is a powerful method for tailoring the physicochemical properties of ZnO without altering its chemical composition. During this process, mechanical energy is transferred into the crystal lattice through repeated impacts between milling media and powder particles.

One of the primary effects of this treatment is the generation of lattice defects. High-energy collisions locally disrupt Zn–O bonds, leading to the formation of oxygen vacancies, dislocations, and partially amorphous regions. These structural defects act as charge trapping centers, promoting efficient charge separation and suppressing electron–hole recombination during the catalytic process. In addition, mechanochemical activation significantly modifies the particle morphology, which is a critical factor in tribocatalysis, as the degradation reactions are predominantly surface-controlled. The increased density of unsaturated surface atoms further enhances surface reactivity and facilitates the generation of reactive oxygen species (ROS).

However, the duration of mechanochemical treatment plays a crucial role in determining the overall catalytic performance. The results indicate that ZnO activated for 1 h exhibits superior degradation efficiency ($D_{glass\ reactor}$ = 86%, $D_{PTFE\ reactor}$ = 93%) compared to the sample treated for 5 h ($D_{glass\ reactor}$ = 81%, $D_{PTFE\ reactor}$ = 88%) at 500 rpm stirring rate (Figure 8). The steeper slope observed in the kinetic profiles for the 1 h sample also suggests a faster degradation rate and improved catalytic activity. Prolonged milling leads

to pronounced particle agglomeration due to the high surface energy of finely divided particles, which promotes re-clustering. Moreover, an excessive concentration of defects may act as recombination centers rather than charge separation sites, thereby reducing catalytic efficiency.



(**a**) (**b**)

Figure 8. Tribocatalytic degradation of Cephalexin using mechanochemically activated ZnO/MeOH and ZnO/EtOH catalysts in (**a**) glass and (**b**) PTFE reactors.

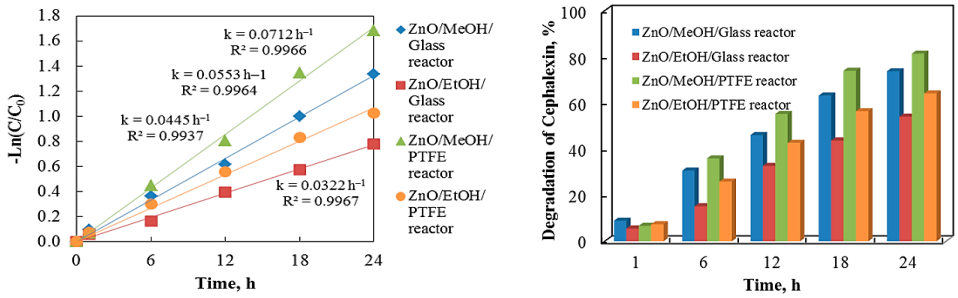
The superior performance of the 1 h mechano-activated ZnO compared to all other investigated systems in cephalexin degradation highlights the critical role of controlled mechanochemical pre-activation in optimizing catalyst properties and maximizing tribocatalytic activity.

3.6. Piezocatalytic Degradation of Cephalexin Using Mechanochemically Activated ZnO Powders

Piezocatalysis involves charge generation through mechanical deformation of piezoelectric materials, typically using inert stirring elements such as glass rods that induce limited mechanical stress and minimal triboelectric effects. In contrast, tribocatalysis is driven by frictional interactions between the catalyst and more triboelectrically active materials, such as PTFE (Teflon) stirring elements, which promote significant charge transfer due to their strong tendency to gain electrons. Consequently, systems employing PTFE anchors exhibit enhanced catalytic performance compared to those using glass anchors, owing to the combined effects of friction-induced charge generation and improved charge separation.

The kinetic profiles of cephalexin degradation over the mechanochemically activated samples (1 h) are presented in Figure 9a as plots of $-\ln(C/C_0)$ versus reaction time. The linear relationships obtained ($R^2 \approx 0.99$) indicate that the process follows pseudo-first-order kinetics under the studied conditions, which is commonly reported for antibiotic degradation in heterogeneous catalytic systems [54]. The calculated apparent rate constants (k) reveal a clear dependence on both the reaction medium and the reactor material. Among the investigated systems, the highest cephalexin degradation efficiency was achieved for the ZnO/MeOH/PTFE reactor system, reaching 81.37%, followed by ZnO/MeOH/Glass reactor with 73.75% degradation. In contrast, lower degradation efficiencies were observed in ethanol-containing systems, namely 64.11% for ZnO/EtOH/PTFE reactor and 54.05% for ZnO/EtOH/Glass reactor (Figure 9b). These results demonstrate that both the solvent nature and reactor composition significantly influence the catalytic performance and degradation efficiency of cephalexin.

The highest rate constant (k = 0.0712 h^{-1}) was observed for the ZnO/MeOH system in a glass reactor, followed by ZnO/MeOH in a PTFE reactor (k = 0.0553 h^{-1}). Lower degradation rates were obtained in ethanol-containing systems, with k values of 0.0445 h^{-1} (glass reactor) and 0.0322 h^{-1} (PTFE reactor), respectively. These results suggest that methanol enhances the degradation efficiency, most likely due to its higher ability to act as a hole scavenger and to promote the formation of reactive oxygen species such as •OH and $\bullet O_2^-$ radicals [33].



(**a**) (**b**)

Figure 9. (**a**) Kinetic plots and (**b**) Piezocatalytic degradation of Cephalexin using mechanochemically activated (1 h) ZnO/MeOH and ZnO/EtOH catalysts.

Despite the observed activity, the piezocatalytic performance of the samples remains inferior compared to their tribocatalytic counterparts (Figure 9). This difference can be attributed to the distinct charge generation mechanisms involved in the two processes. In piezocatalysis, charge carriers are generated through mechanical deformation of the ZnO crystal lattice, leading to polarization and subsequent redox reactions [55]. However, this effect is relatively limited in magnitude and strongly dependent on the extent of applied mechanical stress. In contrast, tribocatalysis involves intensive frictional contact between the catalyst particles and the stirring medium or reactor components, resulting in significant triboelectric charge generation [56]. The use of a PTFE (Teflon) stirring element is particularly important in this context, as PTFE is located at the negative extreme of the triboelectric series and can readily accumulate and transfer electrons during contact [57]. This leads to enhanced charge separation and a higher density of reactive species, ultimately accelerating the degradation process.

The slower kinetics observed in piezocatalytic experiments using a glass stirring element can be explained by the comparatively weak triboelectric properties of glass. Glass is positioned closer to the neutral region of the triboelectric series and therefore generates significantly lower surface charge upon contact. As a result, the reaction relies predominantly on the intrinsic piezoelectric effect of ZnO, which alone is insufficient to achieve high catalytic efficiency. The results demonstrate that while piezocatalysis contributes to cephalexin degradation, the synergistic effects of friction-induced charge generation in tribocatalytic systems—especially in the presence of PTFE components—play a dominant role in enhancing the reaction kinetics.

Building on these observations, radical scavenging (Figure 10) experiments were conducted to elucidate the dominant reactive species and to further compare the underlying mechanisms of piezocatalysis and tribocatalysis. The results confirm that the lower radical generation in piezocatalytic systems is responsible for their reduced degradation efficiency compared to tribocatalytic processes.

The kinetic analysis presented in Figure 9 demonstrates that the degradation of cephalexin follows pseudo-first-order kinetics, with comparatively low apparent rate constants under piezocatalytic conditions. To further clarify the origin of this limited activity, radical scavenging experiments were performed (Figure 10). As illustrated in Figure 10, the addition of ascorbic acid (AA), isopropanol (IPA), and EDTA-2Na, acting as scavengers for superoxide radicals ($\bullet O_2^-$), hydroxyl radicals ($\bullet OH$), and photogenerated holes (h^+), respectively, led to a noticeable decrease in degradation efficiency for both reactor systems.

In the absence of scavengers, the degradation efficiency reached approximately 75–85% in the PTFE reactor and 55–78% in the glass reactor, depending on the catalyst system. The presence of AA caused the strongest inhibition, reducing cephalexin degradation to about 60–68% in the PTFE reactor and 42–60% in the glass reactor. In contrast, IPA and EDTA-

2Na produced a less pronounced suppression, with degradation efficiencies remaining in the ranges of 70–80% and 50–74%, respectively. The stronger inhibitory effect observed in the presence of AA indicates that $\bullet O_2^-$ radicals play a dominant role in the reaction mechanism, whereas •OH radicals and photogenerated holes contribute to a lesser extent. Importantly, the overall moderate suppression of the reaction after scavenger addition suggests a relatively limited generation rate of reactive oxygen species in the piezocatalytic system. This observation is consistent with the kinetic results shown in Figure 9, where lower apparent rate constants were obtained compared to tribocatalytic systems. The correlation between reduced radical formation and slower degradation kinetics confirms that the limited efficiency of piezocatalysis originates from weaker charge generation capability. In contrast, tribocatalysis (Figure 6) benefits from friction-induced charge transfer, which significantly enhances reactive oxygen species formation and accelerates cephalexin degradation.

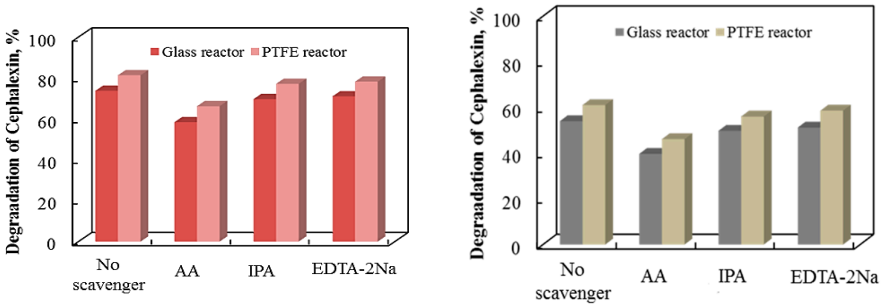


Figure 10. Role of radical scavengers in cephalexin piezocatalytic breakdown by (**a**) ZnO/MeOH and (**b**) ZnO/EtOH catalysts.

3.7. Proposed Mechanism of Tribocatalysis

Figure 11 illustrates the proposed mechanism of tribocatalysis, in which mechanical friction between ZnO catalysts and a PTFE stirring rod induces the generation of triboelectric charges on the surfaces of the contacting materials. Through continuous contact and separation during stirring, charge transfer occurs at the solid–solid interface, resulting in the accumulation of both positive (q^+) and negative (q^-) charges on different regions of the ZnO particle surfaces. This process leads to a spatial separation of charge, governed by local surface states and differences in electron affinity between the interacting materials. The tribogenerated charge carriers subsequently participate in redox reactions at the solid–liquid interface. Positively charged surface sites of ZnO facilitate oxidation reactions involving water molecules, leading to the formation of highly reactive hydroxyl radicals (•OH). These species are among the most powerful oxidants in aqueous systems and play a central role in the degradation of organic contaminants. In parallel, negatively charged regions promote reduction processes by transferring electrons to dissolved oxygen molecules, resulting in the formation of superoxide radicals ($\bullet O_2^-$). The synergistic action of these reactive oxygen species (ROS) enables the progressive breakdown of antibiotic molecules into intermediate products and, ultimately, their complete mineralization into inorganic end-products such as carbon dioxide and water.

In comparison, piezocatalysis is also based on mechanically induced charge generation; however, the underlying mechanism differs fundamentally. In piezocatalytic systems, charge carriers are generated through deformation of piezoelectric materials, where an internal electric field is created as a result of strain-induced polarization. Although this process also leads to the formation of reactive oxygen species, the overall density of generated charges and their spatial separation are typically lower compared to tribocatalytic systems.

As a consequence, piezocatalysis generally produces a smaller quantity of reactive radicals (•OH and $\bullet O_2^-$), which directly results in a reduced catalytic degradation efficiency for pharmaceutical pollutants such as cephalexin. Therefore, tribocatalysis can exhibit superior degradation performance under similar experimental conditions, primarily due to the higher intensity of charge generation and the enhanced formation rate of reactive radical species in the reaction medium.

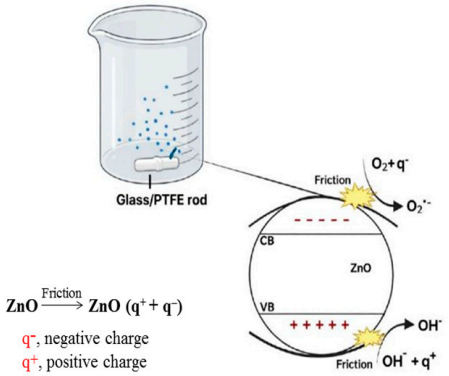


Figure 11. Proposed mechanism of tribocatalysis using ZnO.

4. Conclusions

The present study systematically evaluates ZnO catalysts synthesized by sol–gel and mechanochemical methods for degrading cephalexin under mechanically induced conditions. The results show that catalytic performance is governed by a complex interplay among crystallinity, defect structure, and surface morphology, all of which are strongly influenced by synthesis parameters and post-treatment strategies. In particular, moderate mechanochemical activation (1 h) was identified as optimal because it enhances defect-mediated charge separation while preserving sufficient surface accessibility. A clear distinction between piezocatalytic and tribocatalytic behavior was established, with tribocatalysis showing higher efficiency due to more effective charge generation at solid–solid interfaces. The influence of reactor material further underscores the importance of interfacial phenomena in determining catalytic outcomes. Mechanistic analysis confirmed the predominant role of superoxide radicals, supporting a ROS-driven degradation pathway. Taken together, these findings deepen understanding of structure–function relationships in ZnO-based systems and highlight the potential of mechanically driven catalytic processes as viable and sustainable alternatives for treating antibiotic-contaminated waters.

Author Contributions: Conceptualization, N.K.; methodology, T.T. and N.K.; investigation, T.T., S.T. and N.K.; writing—original draft preparation, T.T. and N.K.; writing—review and editing, N.K. All authors have read and agreed to the published version of the manuscript.

Funding: This research was funded by the Bulgarian NSF project KP-06-N89/07 (КП-06-Н89/07). Research equipment of the Distributed Research Infrastructure INFRAMAT, part of the Bulgarian National Roadmap for Research Infrastructures, supported by the Bulgarian Ministry of Education and Science was used in this investigation.

Data Availability Statement: The original contributions presented in this study are included in the article. Further inquiries can be directed to the corresponding authors.

Acknowledgments: The authors are grateful to financially supported by the Bulgarian NSF project KP-06-N89/07 (КП-06-Н89/07). Research equipment of the Distributed Research Infrastructure INFRAMAT, part of the Bulgarian National Roadmap for Research Infrastructures, supported by the Bulgarian Ministry of Education and Science was used in this investigation.

Conflicts of Interest: The authors declare no conflicts of interest.

References

1. Polianciuc, S.; Gurzău, A.; Kiss, B.; Ştefan, M.; Loghin, F. Antibiotics in the environment: Causes and consequences. *Med. Pharm. Rep.* **2020**, *93*, 232–273. [CrossRef]
2. Alduina, R. Antibiotics and Environment. *Antibiotics* **2020**, *9*, 202. [CrossRef]
3. Mitropoulos, I.; Rotschafer, J.; Rodvold, K. Adverse events associated with the use of oral cephalosporins/cephems. *Diagn. Microbiol. Infect. Dis.* **2007**, *57*, 67S–76S. [CrossRef]
4. Pariatamby, A.; Kee, Y. Persistent organic pollutants management and remediation. *Pers. Org. Pollut. Manag. Remed.* **2016**, *31*, 842–848. [CrossRef]
5. Liu, N.; Wang, R.; Jiawei, Z.; Jiang, J.; Fan, F. Piezoelectricity and triboelectricity enhanced catalysis. *Nano Res. Energy* **2024**, *3*, e9120137. [CrossRef]
6. Ju, M.; Dou, Z.; Li, J.; Qiu, X.; Shen, B.; Zhang, D.; Yao, F.; Gong, W.; Wang, K. Piezoelectric Materials and Sensors for Structural Health Monitoring: Fundamental Aspects, Current Status, and Future Perspectives. *Sensors* **2023**, *23*, 543. [CrossRef]
7. Mahapatra, S.; Mohapatra, P.; Aria, A.; Christie, G.; Mishra, Y.; Hofmann, S.; Thakur, V. Piezoelectric Materials for Energy Harvesting and Sensing Applications: Roadmap for Future Smart Materials. *Adv. Sci.* **2021**, *8*, 2100864. [CrossRef] [PubMed]
8. Deng, K.; Liu, Z.; Liu, H.; Chen, Y.; Li, S.; Guo, S.; Xiu, B.; Dong, X.; Cao, H. Temperature Dependence on Microstructure, Crystallization Orientation, and Piezoelectric Properties of ZnO Films. *Sensors* **2025**, *25*, 242. [CrossRef]
9. Yang, H.; Lee, C.; Lee, J. Piezocatalysis-combined advanced oxidation processes for organic pollutant degradation in water system. *Ultras. Sonochem.* **2025**, *113*, 107219. [CrossRef]
10. Ning, X.; Hao, A.; Cao, Y.; Hu, J.; Xie, J.; Jia, D. Effective promoting piezocatalytic property of zinc oxide for degradation of organic pollutants and insight into piezocatalytic mechanism. *J. Coll. Inter. Sci.* **2020**, *577*, 290–299. [CrossRef] [PubMed]
11. Shen, J.; Wang, K.; Chen, S.; Jiang, H.; Liang, Y.; Tian, X. Boosted low-frequency piezocatalysis in ZnO-CNTs-PVDF membrane: The role of charge migration and interfacial reactive species. *Appl. Catal. Environ. Energy* **2026**, *384*, 126189. [CrossRef]
12. Ivanova, D.; Kolev, H.; Mladeonva, R.; Karakirova, Y.; Kaneva, N. Utilizing Friction Energy on Nanoflowers (Zinc Oxide and Zinc Oxide/Neodymium Oxide) for Tribocatalysis of Doxycycline. *Molecules* **2025**, *30*, 4653. [CrossRef] [PubMed]
13. Chong, J.; Tai, B.; Zhang, Y. Tribocatalysis effect based on ZnO with various specific surface areas for dye degradation. *Chem. Phys. Lett.* **2023**, *835*, 140998. [CrossRef]
14. Che, J.; Jia, Y.; Gao, Y.; Wang, X.; Wu, Z.; Ma, J.; Wang, Z.; Liu, C. Review on tribocatalysis through harvesting friction energy for mechanically-driven dye decomposition. *J. All. Comp.* **2024**, *1002*, 175413. [CrossRef]
15. Xiao, L.; Xu, X.; Wu, Z.; Sun, T.; He, X.; Xu, X.; Qin, L.; Chen, D. Recent progress and prospect of friction-driven-tribocatalysis: From basic principle to material design. *Surf. Int.* **2025**, *56*, 105557. [CrossRef]
16. Kajdasa, C.; Kulczycki, A.; Ozimina, D. A new concept of the mechanism of tribocatalytic reactions induced by mechanical forces. *Tribol. Int.* **2017**, *107*, 144–151. [CrossRef]
17. Roslan, N.; Lau, H.; Suhaimi, N.; Usman, A. Recent Advances in Advanced Oxidation Processes for Degrading Pharmaceuticals in Wastewater—A Review. *Catalysts* **2024**, *14*, 189. [CrossRef]
18. Wang, J.; Zhuan, R. Degradation of antibiotics by advanced oxidation processes: An overview. *Sci. Total Environ.* **2020**, *701*, 135023. [CrossRef]
19. Jiang, Y.; Liang, J.; Zhuo, F.; Ma, H.; Mofarah, S.; Sorrell, C.; Wang, D.; Koshy, P. Unveiling Mechanically Driven Catalytic Processes: Beyond Piezocatalysis to Synergetic Effects. *ACS Nano* **2025**, *19*, 18037–18074. [CrossRef]
20. Wu, J.; Qin, N.; Bao, D. Effective enhancement of piezocatalytic activity of $BaTiO_3$ nanowires under ultrasonic vibration. *Nano Energy* **2018**, *45*, 44–51. [CrossRef]
21. Fan, F.; Xie, S.; Wang, G. Tribocatalysis: Challenges and perspectives. *Sci. China Chem.* **2021**, *64*, 1609–1613. [CrossRef]
22. Xie, Y.; Zhu, M.; Xu, Z.; Bing, L.; Chen, W.; Shen, Z. Strong Tribocatalytic Degradation of Organic Pollutants by Natural Shell Particles. *Nanomaterials* **2026**, *16*, 194. [CrossRef] [PubMed]
23. Yu, H.; Zhu, X.; Zhao, Z.; Sui, X.; Sun, S.; He, X.; Zhang, Y.; Ye, W. Tribocatalytic Degradation of Organic Pollutants Using Fe2O3 Nanoparticles. *ACS Appl. Nano Mater.* **2023**, *6*, 14364–14373. [CrossRef]
24. Zhu, H.; Zhou, Z.; Ke, S.; Mao, C.; Song, J.; Chen, W. Tribocatalytic Degradation of Organic Dyes by Disk-Shaped PTFE and Titanium: A Powder-Free Catalytic Technology for Wastewater Treatment. *Catalysts* **2025**, *15*, 754. [CrossRef]
25. Lei, H.; Cui, X.; Jia, X.; Qi, J.; Wang, Z.; Chen, W. Enhanced Tribocatalytic Degradation of Organic Pollutants by ZnO Nanoparticles of High Crystallinity. *Nanomaterials* **2023**, *13*, 46. [CrossRef] [PubMed]
26. Ong, C.; Ng, L.; Mohammad, A. A Review of ZnO Nanoparticles: Synthesis and Applications. *Renew. Sustain. Energy Rev.* **2018**, *81*, 536–551. [CrossRef]
27. Luo, Y.; Wu, Y. Defect Engineering in ZnO Nanomaterials for Enhanced Catalysis. *Appl. Catal. Environ.* **2023**, *13*, 1116. [CrossRef]

28. Lysak, A.; Wierzbicka, A.; Dłużewski, P.; Stachowicz, M.; Sajkowski, J.; Przezdziecka, E. Influence of the Annealing Temperature on the Properties of {ZnO/CdO}30 Superlattices Deposited on c-Plane Al2O3 Substrate by MBE. *Crystals* **2025**, *15*, 174. [CrossRef]
29. Carta, M.; Colacino, E.; Delogu, F.; Porcheddu, A. Kinetics of mechanochemical transformations. *Phys. Chem. Chem. Phys.* **2020**, *22*, 14489. [CrossRef]
30. Zhang, J.; Li, J. The Oxygen Vacancy Defect of ZnO/NiO Nanomaterials Improves Photocatalytic Performance and Ammonia Sensing Performance. *Nanomaterials* **2022**, *12*, 433. [CrossRef]
31. Dong, H.; Zhou, Y. Oxygen Vacancies in Piezocatalysis: A Critical Review. *Chem. Eng. J.* **2024**, *487*, 150480. [CrossRef]
32. Lu, X.; Zhang, R.; Liu, Y.; Zhou, Z.; Xia, Y.; Wang, J.; Guo, Y.; Fan, X. Oxygen Vacancies and Lattice Distortion in Piezocatalysis. *ACS Appl. Mater. Int.* **2024**, *16*, 63692–63702. [CrossRef]
33. Nosaka, Y.; Nosaka, A. Generation and Detection of Reactive Oxygen Species in Photocatalysis. *Chem. Rev.* **2017**, *117*, 11302–11336. [CrossRef]
34. Yang, Y.; Zhang, Y.; Fernandez-Alberti, S.; Long, R. Resolving the Puzzle of Charge Carrier Lifetime in ZnO by Revisiting the Role of Oxygen Vacancy. *J. Phys. Chem. Lett.* **2024**, *15*, 1–8. [CrossRef]
35. Ribeiro, A.; Sures, B.; Schmidt, T. Cephalosporin antibiotics in the aquatic environment: A critical review of occurrence, fate, ecotoxicity and removal technologies. *Environ. Pollut.* **2018**, *241*, 1153–1166. [CrossRef] [PubMed]
36. Das, N.; Madhavan, J.; Selvi, A.; Das, D. An overview of cephalosporin antibiotics as emerging contaminants: A serious environmental concern. *3 Biotech* **2019**, *9*, 231. [CrossRef] [PubMed]
37. Patterson, A. The Scherrer formula for X-ray particle size determination. *Phys. Rev.* **1939**, *56*, 978–982. [CrossRef]
38. Rai, R.; Bajpai, V. Recent advances in ZnO nanostructures and their future perspective. *Adv. Nano Res.* **2021**, *11*, 037–054. [CrossRef]
39. Djurišić, A.; Ng, A.; Chen, X. ZnO nanostructures for optoelectronics: Material properties and device applications. *Progr. Quantum Electr.* **2010**, *34*, 191–259. [CrossRef]
40. Kuriakose, S.; Satpati, B.; Mohapatra, M. Effects of Solvent on Structural, Optical and Photocatalytic Properties of ZnO Nanostructures. *Adv. Mater. Lett.* **2015**, *6*, 1104–1110. [CrossRef]
41. Shnain, Z.; Toma, M.; Abdulhussein, B.; Saleh, N.; Ibrahim, M.; Manuel, N.; Mahmood, A. The Effect of Solvent-Modification on the Physicochemical Properties of ZnO Nanoparticles Synthesized by Sol-Gel Method. *Bull. Chem. React. Eng. Catal.* **2022**, *17*, 46–52. [CrossRef]
42. Baláž, P. Mechanochemistry in nanoscience and minerals engineering. In *Mechanochemistry in Nanoscience and Minerals Engineering*; Springer: Berlin/Heidelberg, Germany, 2008. [CrossRef]
43. James, S.; Adams, C.; Bolm, C.; Braga, D.; Collier, P.; Friščić, T.; Grepoini, F.; Harris, K.; Hyett, G.; Jones, W.; et al. Mechanochemistry: Opportunities for new and cleaner synthesis. *Chem. Soc. Rev.* **2012**, *41*, 413–447. [CrossRef]
44. Senna, M. The Optimization of Mechanochemical Processes toward Functional Nanocomposite Materials. *Powders* **2023**, *2*, 659–677. [CrossRef]
45. Zhou, Z.; Wang, J.; Jhun, C. ZnO Nanospheres Fabricated by Mechanochemical Method with Photocatalytic Properties. *Catalysts* **2021**, *11*, 572. [CrossRef]
46. Motelica, L.; Vasile, B.; Ficai, A.; Surdu, A.; Ficai, D.; Oprea, O.; Andronescu, E.; Jinga, D.; Holban, A. Influence of the Alcohols on the ZnO Synthesis and Its Properties: The Photocatalytic and Antimicrobial Activities. *Pharmaceutics* **2022**, *14*, 2842. [CrossRef]
47. Ungula, J.; Dejene, B. Effect of solvent medium on the structural, morphological and optical properties of ZnO nanoparticles synthesized by the sol–gel method. *Phys. Condens. Matter* **2016**, *480*, 26–30. [CrossRef]
48. Rezapour, M.; Talebian, N. Comparison of structural, optical properties and photocatalytic activity of ZnO with different morphologies: Effect of synthesis methods and reaction media. *Mater. Chem. Phys.* **2011**, *129*, 249–255. [CrossRef]
49. Ali, A.; Ambreem, S.; Javed, R.; Tabassum, S.; Haq, I.; Zia, M. ZnO nanostructure fabrication in different solvents transforms physio-chemical, biological and photodegradable properties. *Mater. Sci. Eng.* **2017**, *74*, 137–145. [CrossRef]
50. Zeid, S.; Leprince-Wang, Y. Advances in ZnO-Based Photocatalysts for Water Treatment. *Crystals* **2024**, *14*, 611. [CrossRef]
51. Mohamed, K.; Benitto, J.; Vijaya, J.; Bououdina, M. Recent Advances in ZnO Nanostructures for Photocatalytic Degradation of Pharmaceuticals. *Crystals* **2023**, *13*, 329. [CrossRef]
52. Abdeyazdan, Z.; Rahmati, M.; Mehrabani-Zeinabad, A.; Zare, M. Design, synthesis, and optimization of a novel ternary photocatalyst for degradation of cephalexin antibiotic in aqueous solutions. *Sci. Rep.* **2025**, *15*, 8824. [CrossRef]
53. Luo, J.; Wang, Z. Recent progress of triboelectric nanogenerators: From fundamental theory to practical applications. *EcoMat* **2020**, *2*, e12059. [CrossRef]
54. Chong, M.N.; Jin, B.; Chow, C.W.K.; Saint, C. Recent developments in photocatalytic water treatment technology: A review. *Water Res.* **2010**, *44*, 2997–3027. [CrossRef] [PubMed]
55. Hong, K.; Xu, H.; Konishi, H.; Li, X. Direct water splitting through vibrating piezoelectric microfibers in water. *J. Phys. Chem. Lett.* **2010**, *1*, 997–1002. [CrossRef]

56. Lin, S.; Xu, L.; Wang, Z.L. Triboelectric nanogenerators: From fundamental principles to advanced applications. *Adv. Mater.* **2020**, *32*, 1903799. [CrossRef]
57. Zou, H.; Zhang, Y.; Guo, L.; Wang, P.; He, X.; Dai, G.; Zheng, H.; Chen, C.; Wang, A.C.; Xu, C.; et al. Quantifying the triboelectric series. *Nat. Commun.* **2019**, *10*, 1427. [CrossRef]

Disclaimer/Publisher's Note: The statements, opinions and data contained in all publications are solely those of the individual author(s) and contributor(s) and not of MDPI and/or the editor(s). MDPI and/or the editor(s) disclaim responsibility for any injury to people or property resulting from any ideas, methods, instructions or products referred to in the content.